XAFS atomistic insight of the oxygen gettering in Ti/HfO_2 based OxRRAM

R. Viennet, H. Roussel, L. Rapenne, J. L. Deschanvres, and H. Renevier*
Université Grenoble Alpes, CNRS, Grenoble INP, LMGP, F-38000 Grenoble, France

V. Jousseaume and E. Jalaguier
Université Grenoble Alpes, F-38000 Grenoble, France
and CEA, LETI, MINATEC Campus, F-38054 Grenoble, France

M. G. Proietti
Departamento de Fisica de la Materia Condensada, Instituto de Ciencia de Materiales de Aragon, CSIC-Universidad de Zaragoza, Spain

(Received 12 July 2017; revised manuscript received 13 January 2018; published 11 May 2018)

Hafnia-based resistive memories technology has come to maturation and acceded to the market of nonvolatile memories. Nevertheless, the physical mechanisms involved in resistive switching are not yet fully understood and the numerous *ab initio* simulations studies have few many atomic-scale experimental counterparts. In this study we investigate the oxygen migration mechanism from an amorphous HfO_2 layer to the Ti cap layer at a local scale before and after a thermal treatment. X-ray absorption spectroscopy at the Ti K edge and Hf L_{III} edge has been performed on samples as-deposited and annealed in Ar at 400 °C to mimic the back-end-of-line thermal budget (BEOL) of CMOS technology. The short-range Ti and Hf environments have been determined, showing that annealing promotes the migration of O from HfO_2 to Ti, the amount of which is quantified. This provokes an expansion and an increase of atomic disorder in the Ti lattice. The nature of the oxygen gettering mechanism by the Ti metal is understood by comparing samples with increasing Ti-capping thickness. We show that the Ti getter effect has to be activated by thermal treatment and that the O diffusion takes place in a region of a few nanometers close to the Ti/HfO_2 interface. Therefore, the thermal budget history and the Ti cap-layer thickness determine the oxygen vacancy content in the HfO_2 layer, which in turn controls the electrical properties, especially the forming operation.

DOI: 10.1103/PhysRevMaterials.2.055002

I. INTRODUCTION

Oxide resistive random access memories (OxRRAMs) are based on the reversible voltage-controlled resistance switching [1] from a high resistive state (HRS) to a low resistive state (LRS). They have been recognized as a serious opportunity for the next generation of nonvolatile memories with device sizes below the 20 nm technological node [2]. Among the reported switchable oxides, Hafnia (HfO_2) has raised a lot of interest, partly because of its long-term use in the micro-electronics industry as a gate dielectric in silicon complementary metal oxide semiconductor (Si CMOS) transistors [3–6]. In addition, it is known that the nature of the top and bottom electrodes has a great impact on the OxRRAM electrical performance [7,8]. Hafnia associated with a titanium [9–11] active top electrode constitutes one of the best metal-oxide-metal (MIM) capacitors for resistive switching memories. The latter have demonstrated an excellent electrical behavior with low voltage set and reset, high writing speed, and a long retention of information [12,13]. In the last decade, a great deal of basic research on HfO_2-based RRAM switching mechanism was focused on understanding the electric-field-induced physical chemistry occurring during voltage cycling. It is now widely accepted that reversible resistive switching, caused by the application of an electric field [7,14,15], results in the formation and disruption of a conductive filament between both electrodes. Electrical [16,17], physico-chemical [9,18] and *ab initio* [19] studies point out oxygen vacancy clustering as the origin of the conductive filament. The Ti top electrode acts as an oxygen reservoir [20–22], playing a major role in HfO_2 switching and being compatible with the final electrical interconnection step of device fabrication (back end of line, or BEOL) process. The capping metal oxygen getter generates oxygen vacancies, which leads to a higher leakage current prior to the forming, which in turn results in a lower voltage for initiating the breakdown process [23]. After forming, the most accepted scenario, although still controversial [15,24], is that the metal cap (reactive electrode) serves as a reservoir for defect migration during the set and reset.

In this study, we focus on the Ti/HfO_2 interface and aim to quantitatively determine and correlate the oxygen atoms and oxygen vacancies (V_O) amounts in Ti top and HfO_2 layers, respectively, in as-deposited (AD) and annealed (Ann) pristine samples with a varying Ti thickness and a constant HfO_2 thickness (10 nm). The annealing was performed to mimic the thermal budget of BEOL. The latter has a fundamental impact on the device electrical properties because it determines the number of oxygen atoms gettered by the Ti electrodes from the HfO_2 layer, prior to the forming operation. Basically,

*hubert.renevier@grenoble-inp.fr

 ©2018 American Physical Society

the Ti metal oxygen scavenging relies on the thermodynamic reaction of Ti in α-Ti with oxygen in HfO_2. It depends on the oxygen diffusion kinetic through the Ti/HfO_2 interface and the α-Ti interstitial sites [10,20,24–26] and, ultimately, the possible Ti suboxides are given by the Ti-O thermodynamic phase diagram [27]. Here, we report on the results of x-ray absorption spectroscopy (XAS) performed at both the Ti K and Hf L_{III} edges. XAFS has the ability to probe the density of states (DOS) of empty states above the Fermi level and the local environment of the absorbing atom. It has allowed us to quantify the O coordination number in the nearest coordination shell of Ti and Hf as well as the Ti-O and Ti-Ti interatomic distances [28]. It is particularly suitable to determine the structural properties of this system since x-ray diffraction cannot give information due to the amorphous nature of the HfO_2 layer and the mixed amorphous or short-range-ordered nature of the Ti layers. This study experimentally determines the migration mechanism of O atoms from HfO_2 to the Ti electrode due to the thermal budget.

II. SAMPLES

HfO_2 layers (10 nm thick) were grown by atomic layer deposition (ALD) on Si(100) substrates at 350 °C from $HfCl_4$ and H_2O precursor and oxidant [29]. A Ti top electrode of variable thickness (5 to 40 nm) followed by a 40-nm-thick Pt layer were deposited by thermal evaporation at room temperature in a 10^{-7} torr vacuum onto the HfO_2 layers. To mimic the thermal budget of BEOL, we defined two series of samples: as deposited (AD) and annealed (Ann) one hour at 400 °C under a flowing argon atmosphere.

Transmission electron microscopy (TEM) observations were carried out at 200 kV with a JEOL 2010 microscope (resolution of 0.19 nm) on as-deposited and annealed samples. X-ray energy dispersive spectra and mapping were collected by scanning TEM using a JEOL 2100F FEG microscope operating at 200 kV and equipped with the JEOL SDD Centurio detector. Cross-section samples were prepared with a thin wedge shape by means of automated tripod polishing using the MultiPrep^{TM}system (Allied High Tech Products, Inc.) and using plastic diamond lapping films with grains of decreasing size (15–0.5 μm). The final polishing was done on a soft felt-covered disk impregnated with a silica solution until the apparition of the first extinction fringe among those of equal thickness. Ar-ion milling was applied for several minutes to optimize the thickness. Figures 1(a) and 1(b) show the cross sections of the Ti 10 nm as-deposited and annealed samples, respectively. One can observe that the HfO_2 layer is amorphous both before and after annealing because no crystalline region or grains are visible. This is due the low deposition temperature and layer thickness and, clearly, the annealing (one hour at 400 °C under a flowing argon atmosphere) does not induce crystallization. In the Ti layer one can see randomly oriented atomic planes together with amorphous regions. No crystal grains are visible. Regarding the interfaces, Figs. 1(a) and 1(b) show that annealing has no detectable effect on the sharpness of the Ti/HfO_2 interfaces. On the contrary, the Pt/Ti interface is enlarged, indicating some atomic interdiffusion. The same conclusion can be drawn from element mapping by x-ray energy dispersive spectroscopy [see Figs. 1(c) and 1(d)]

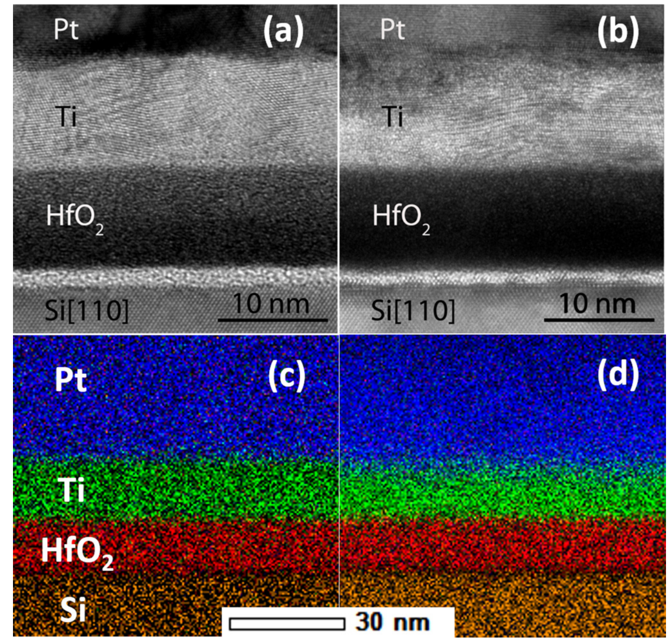

FIG. 1. Transmission electron microscopy cross sections in samples Ti-10 nm (a) as deposited (AD) and (b) annealed (Ann). The thin layer at the interface of silicon and HfO_2 corresponds to amorphous SiO_2. X-ray energy dispersive spectroscopy element mapping of Si, Hf, Ti, and Pt in samples Ti 10 nm (c) AD and (d) Ann.

and x-ray reflectivity (XRR) measurements performed at the ESRF (BM2-D2AM beamline) in the Q range 0–0.15 Å^{-1} (not shown). XRR shows that the HfO_2 thickness and the root mean square stay constant ($\sigma^2 \simeq 0.3$ nm^2), whereas some intermixing occurs instead at the Pt/Ti interface after annealing. Besides, in-plane x-ray diffraction performed on the Ti 40 nm and Ti 0 nm samples before and after annealing revealed that Ti and HfO_2 layers are amorphous; that is, no atomic long-range order was observed.

III. X-RAY ABSORPTION FINE STRUCTURE

The XAFS spectra were recorded at the Hf L_{III} edge (9561 eV) and Ti K edge (4966 eV), at room temperature in fluorescence mode by using a Canberra^{TM} 30-element Ge detector, at beamline BM30B of the ESRF. The fluorescence yield was detected in the horizontal plane at 90° with respect to the x-ray-beam direction. The spectra were recorded by orienting the sample surface nearly parallel to the incident beam (incidence angle equal to about 5°). In such a way the x-ray photon polarization vector $\vec{\varepsilon}$ was nearly perpendicular to the sample surface, which maximizes the sensitivity to out-of-plane bonds perpendicular or nearly perpendicular to the sample interfaces. Note that, for a 10-nm-thick (20 nm-thick) HfO_2 (Ti) layer, the effective thickness is about 115 nm (220 nm), which is much smaller than the absorption length for an energy right above the Hf L_{III} edge (Ti K edge), which is about 4.5 μm (3 μm). Therefore the XAFS spectra were not corrected for self-absorption. The XAFS spectra can be split out in two regions: the near-edge structure (XANES) region spanning from the pre-edge region to 30–50 eV above the absorption edge, and the extended-fine-structure region (EXAFS)

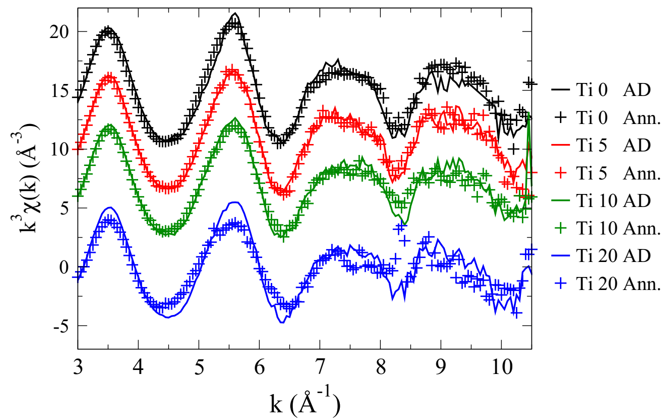

FIG. 2. Raw $k^3\chi(k)$ EXAFS spectra at the Hf L_{III} edge of the as-deposited (AD, continuous curves) and annealed samples (Ann, crosses) for the different Ti cap-layer thicknesses. The spectra are shifted along the y axis for clarity.

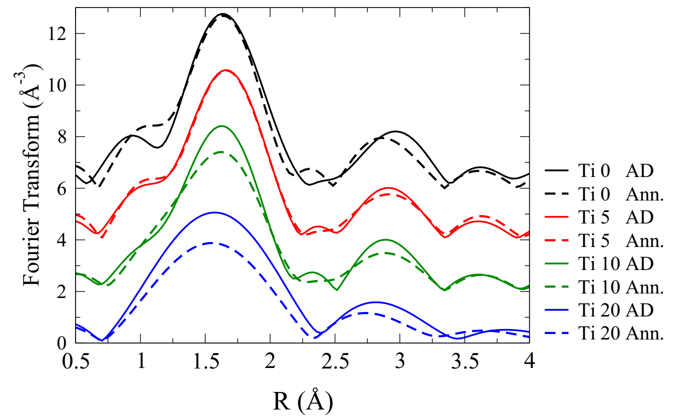

FIG. 3. FT amplitude of $k^3\chi(k)$ EXAFS signals at the Hf L_{III} edge of the as-deposited (AD, continuous curves) and annealed samples (Ann, broken curves) for the different Ti cap-layer thicknesses. The spectra are shifted along the y axis for clarity. The transformation interval was from 3–9.7 Å^{-1} for the 0-, 5-, and 10-nm-thick Ti-layer samples and 3–7 Å^{-1} for the Ti 20 nm thick.

ranging from 30–50 eV up to 1000 eV above the absorption edge. In the EXAFS region, the fine-structure oscillations can be interpreted quantitatively in terms of a scattering path development formalism including single scattering (SS) and multiple scattering (MS) paths for the emitted photoelectron with the neighboring atoms. In this way, using a fitting procedure of the experimental oscillations to a theoretical model calculated by using *ab initio* theoretical phases and amplitudes, the local structure parameters of the system, such as interatomic distances, coordination numbers, and static and thermal disorder factors, can be obtained. EXAFS is complementary to XRD in providing average short- and medium-range order structural information and is particularly suitable for amorphous systems for which diffraction cannot give information. In the XANES region, the path development formalism is no longer valid and inversion of the scattering matrix is needed in the *ab initio* calculations. Full multiple scattering (FMS) simulations must be carried out and the XANES cannot be parametrized and refined as EXAFS. Nevertheless, XANES is very sensitive both to the local atomic arrangement and electronic structure of the system and a simple fingerprint analysis can provide a valuable insight into the changes of the local and electronic environment, as we show in the following.

A. Extended x-ray absorption fine structure of as-deposited and annealed Ti/HfO_2 samples at Hf L_{III} edge

We show in Figs. 2 and 3 the background-subtracted EXAFS oscillations and their Fourier transforms (FTs), respectively, at the Hf L_{III} edge, for the Ti 5 nm, Ti 10 nm, and Ti 20 nm, as-deposited and annealed set of samples. The EXAFS spectrum of an HfO_2 sample grown with no Ti cap layer is also reported as a reference. We observe in all the FT amplitude the first coordination shell corresponding to the Hf oxygen first neighbors (shell I) and a second shell, with a much lower intensity, corresponding, as we show in the following, both to Hf and O next-nearest neighbors. We can see that the addition of Ti as a cap layer, without any thermal treatment, does not produce any noticeable change both in the position (first coordination shell distance) and in the FT peak amplitude pointing to, as expected, the lack of significant variations in the HfO_2 local structure upon Ti cap deposition at room temperature. It has to be noticed that, as specified in the figure caption and shown in Fig. 3, the Ti 20 nm spectrum is available in a narrower energy range due to experimental distortions. This renders the FT spectrum not actually comparable with the rest, with the first-shell contribution being less intense and wider due to the limited transformation range.

The comparison with the annealed samples (dashed curves in Fig. 3) shows instead a clear amplitude lowering of the first coordination shell (O atoms) FT peak upon increasing of the Ti cap-layer thickness and also a shift towards low R values of the peak position. We report hereafter a quantitative analysis of the Hf first coordination shell that will be compared with the quantitative analysis of the EXAFS spectra at the Ti K edge to extract information about the local Hf environment and oxygen diffusion. We show that oxygen diffusion into the Ti layer takes place upon annealing and that it depends on the Ti cap-layer thickness. Further information could be obtained by the analysis of the second coordination shell but we limit here the discussion to a qualitative analysis because the limited k range and signal-to-noise ratio do not allow more complex data refinement. Furthermore, the second shell contributions, due to Hf-Hf and Hf-O single scattering paths and to Hf-O-O three-leg paths, are smeared out by the static disorder due to the amorphous nature of the HfO_2 layers. EXAFS analysis has been performed by comparing the experimental $\chi(k)$ raw spectra with theoretical signals obtained by *ab initio* phases and amplitudes calculations performed by the FEFF8 code [30]. Scattering potentials were calculated in the muffin-tin approximation in a self-consistent way, with a Hedin–Lundqvist approximation for exchange and inelastic losses. Background subtraction in the EXAFS region was performed by AUTOBK code implemented by the ATHENA graphical interface [31]. Fit of theoretical signal to EXAFS was performed by using the IFEFFIT8 code implemented by the ARTEMIS interface [31]. In the SS approximation the EXAFS spectrum can be expressed

as follows:

$$\chi(k) = S_0^2 \sum_j \frac{N_j f_j(k,r_j)}{kr_j^2} e^{-2k^2\sigma_j^2} \sin[2kr_j + \Phi_j(k)], \quad (1)$$

where j is the jth atomic shell, r_j and N_j are the interatomic distance and the effective coordination number, σ_j^2 is the XAFS Debye Waller and quantifies the bond-length disorder (static and dynamic), S_0^2 is the EXAFS amplitude reduction factor due to multi-electron excitation channels, $\Phi_j(k) = \varphi_j(k) + 2\delta$ where φ_j and f_j are the phase shift and the backscattering amplitude of atoms in shell j, δ is the phase shift due to the central atom and k is the photoelectron wave number.

Although HfO_2 is amorphous according to TEM and x-ray diffraction, a crystalline model made by a 6 Å radius cluster was built up by the ATOMS code [33] starting from the monoclinic space group $P2_1/c$ [32,34,35]. This symmetry is known to be more likely than the tetragonal one for this system [36,37]. In addition, the second shell shape, which is a sort of fingerprint for monoclinic and tetragonal symmetry, suggests the use of the monoclinic model [36]. According to it, each Hf central atom is surrounded by seven O atoms with Hf-O interatomic distances ranging from 2.03 to 2.25 Å, as reported in Table I. We also included further single and multiple (three paths) scattering paths (SS) that we found to contribute to the second peak in the FT spectrum appearing in the region from about 2.4 to 3.4 Å (without central-atom phase-shift corrections). They are 5 SS paths Hf-Hf with interatomic distances equal to 3.31, 3.42, 3.44, 3.45, and 3.57 Å; one Hf-O SS path at 3.55 Å; 3 MS Hf-O-O paths at about 3.39 Å; 5 Hf-O-O MS paths with a distance ranging from 3.47 to 3.53 Å. We refined first the I shell contribution, comprising all seven O atoms, by iterating the following parameters: the origin of photoelectron energy, E_0, the interatomic Hf-O distances for the I shell, the XAFS Debye–Waller (DW) factors σ^2, and the S_0^2 amplitude reduction factor. For the E_0 best-fit values, differences less than 0.5 eV were found for the different samples. Due to the low symmetry degree of the monoclinic HfO_2 structure, the 7 NN oxygen atoms show a considerable spread in distances, ranging from 2.03 to 2.25 Å and we refined a unique ΔR value for all these SS paths.

TABLE I. Best-fit values, E_0, S_0^2, ⟨Hf-O⟩ (the average value of the seven Hf-O distances in the I shell) and XAFS Debye–Waller factor σ^2, for the as-deposited (AD) and annealed (Ann) set of samples. Errors have been obtained from the diagonal of the fit covalence matrix. They are equal or lower than 0.02 Å for interatomic distances, 1 eV for E_0 and 0.002 Å^2 for σ^2 (Ti-O) and σ^2 (Ti-Ti).

Samples	E_0	S_0^2	⟨Hf-O⟩ (Å)	σ^2 (Hf-O) (Å^2)
m-HfO_2 P2$_1$/c ([32])			2.14	
Ti 0 nm AD			2.09	0.007
Ti 5 nm AD	0.0	0.94	2.09	0.006
Ti 10 nm AD	0.0	0.94	2.09	0.001
Ti 20 nm AD	0.0	0.94	2.08	0.005
Ti 40 nm AD	0.0	0.94	2.09	0.005
Ti 0 nm Ann	−1.0	0.92	2.09	0.007
Ti 5 nm Ann	−0.9	0.89	2.10	0.007
Ti 10 nm Ann	−1.9	0.80	2.08	0.004
Ti 20 nm Ann	−1.1	0.67	2.08	0.009

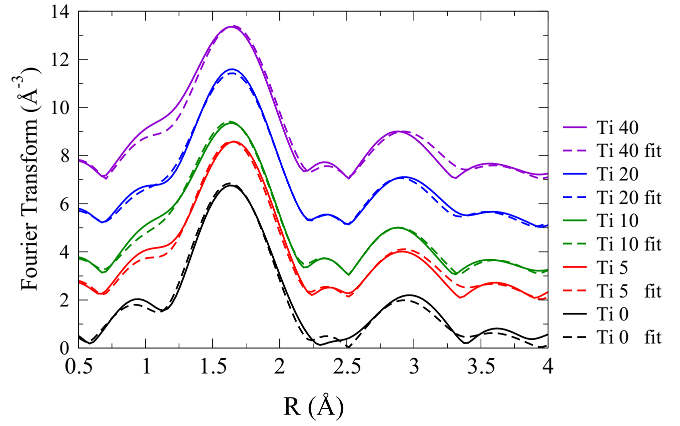

FIG. 4. Best-fit results at the Hf L_{III} edge for the as-deposited (AD) samples (broken curves) compared with the experimental FT signals (continuous curves). The spectra are shifted along the y axis for clarity.

Fits were performed in R space in the range [1–3.7 Å]. Once a good agreement was found for the oxygen I shell contribution, we introduced the further Hf-Hf, Hf-O, and Hf-O-O paths showing to be relevant to obtain a qualitative theory-experiment agreement for the second FT peak. We simplified the fit of this part of the spectrum according to its qualitative character due to its limited k range and large static XAFS Deby–Waller factors due to disorder. We added a minimum number of extra fit parameters by attributing the same XAFS DW factor and ΔR value to paths having similar lengths. This gives two XAFS DW factors and three ΔR values parameters. The best-fit values are reported in Table I and the best-fit curves are reported in Figs. 4 and 5 for the as-deposited and annealed samples, respectively. We observe that the Hf-O interatomic distances show a general decrease of about 0.04–0.06 Å compared with those of the crystalline monoclinic structure reported in Table I, both in the as-deposited and annealed samples, corresponding to an

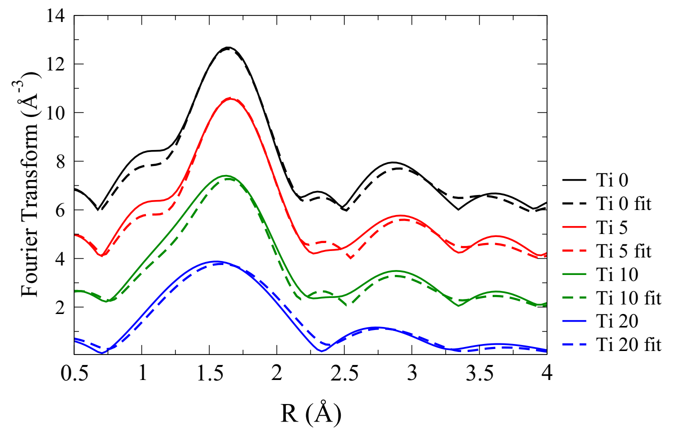

FIG. 5. Best-fit results at the Hf L_{III} edge for the annealed (Ann) samples (broken curves) compared with the experimental FT signals (continuous curves). The spectra are shifted along the y axis for clarity.

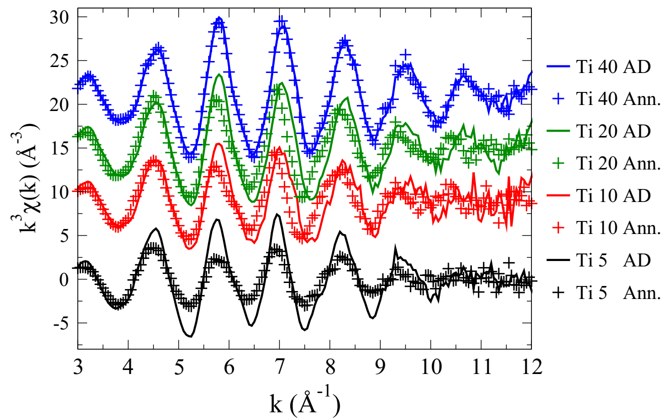

FIG. 6. Raw $k^3\chi(k)$ EXAFS spectra at the Ti K edge of the as-deposited (AD, continuous curves) and annealed samples (Ann, crosses) for the different Ti cap-layer thicknesses. The spectra are shifted along the y axis for clarity.

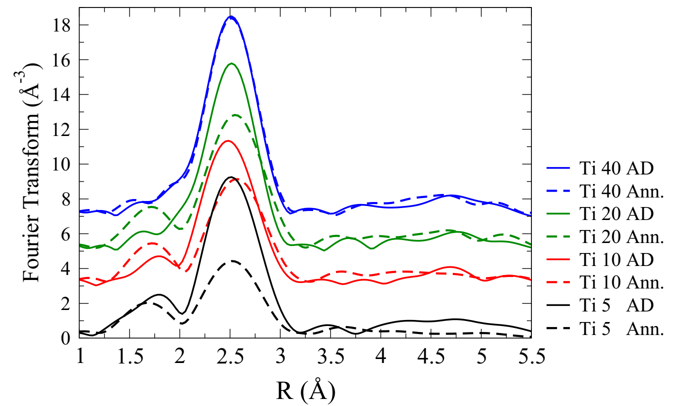

FIG. 7. FT spectra of $k^3\chi(k)$ EXAFS spectra at the Ti K edge of the as-deposited (AD, continuous curves) and annealed samples (Ann, broken curves) for the different Ti cap-layer thicknesses. The spectra are shifted along the y axis for clarity. The transformation interval was 2.8–10.5 Å^{-1}.

average variation of about 2%. This decrease can be related to the amorphous nature of the samples in which the monoclinic lattice is clearly distorted [38]. The same amplitude is found for all the samples, equal to $S_0^2 = 0.94$, before annealing. We made use of the amplitude factor S_0^2, as a fitting parameter reflecting the overall number of the Hf-O pairs. It shows that the Hf oxygen coordination is barely affected, as can be expected, by increasing the thickness of the Ti capping for the as-deposited samples. Concerning the same samples after annealing, we notice a decrease of the Hf-O amplitude factor, from $S_0^2 = 0.92$, for the uncapped sample, to 0.67 for the Ti 20 nm sample. This shows that thermal treatment activates oxygen diffusion to the Ti capping and we also obtain a quantitative estimation of this gettering effect. If we consider that the amplitude is directly proportional to O coordination number, we obtain a decrease of approximately 28%, corresponding to an average loss of about two oxygen atoms out of seven nearest neighbors of the Hf absorber. To confirm this finding we performed EXAFS measurements at the Ti K edge to detect and quantify the oxygen diffusion in the Ti cap layer.

B. Extended x-ray absorption fine structure of as-deposited and annealed Ti/HfO_2 samples at Ti K edge.

We show in Figs. 6 and 7 the background-subtracted EXAFS oscillations and their Fourier transforms (FTs), respectively, at the Ti K edge, for the Ti 5 nm, Ti 10 nm, and Ti 20 nm, as-deposited and annealed set of samples.

We observe only one main contribution corresponding to the Ti-Ti absorber-scatterer pairs and a low-R side peak appearing in the spectra of the Ti 5 nm, Ti 10 nm, and Ti 20 nm thick Ti layer samples corresponding to Ti-O pairs. No further coordination Ti or O shells are found, in agreement with the disordered nature of the Ti cap layers. Regarding the as-deposited samples, we observe a clear trend upon increasing the Ti cap-layer thickness. We see a low-R side peak appearing in the Ti 5 nm and Ti 10 nm samples that points to the presence, as we show in the following, of O atoms in the Ti local environment. This contribution does not show up in the Ti 20 nm and Ti 40 nm samples. If we compare with the annealed samples we observe that, after annealing, the O contribution increases and shows up also in the Ti 20 nm sample. This first qualitative analysis shows that, in the as-deposited samples, an interface oxygen diffusion mechanism takes place in a few-nanometer-scale layer that can be observed only for the low Ti layer thicknesses. Due to the thermal annealing, O atoms are gettered by the Ti layer and diffuse from the interface region to a more extended layer region. We also observe a clear shift to higher R of the interatomic Ti-Ti distance upon annealing for the Ti 10 and Ti 20 nm samples, in agreement with the increase in O diffusion to interstitial sites of the Ti lattice. Quantitative analysis of the EXAFS signals was done according the scheme previously described at the Hf edge. We calculated theoretical phases and amplitudes for a crystalline model made by a 6-Å-radius cluster of hexagonal α-Ti (space group $P\frac{6_3}{m}mc, a = 5.5755$ Å, $c = 8.8503$ Å) containing O atoms in all-octahedral interstitial sites. Indeed, according to Sec. IV and previous literature, the octahedral sites are energetically more favored compared with the possible tetrahedral sites [20]. According

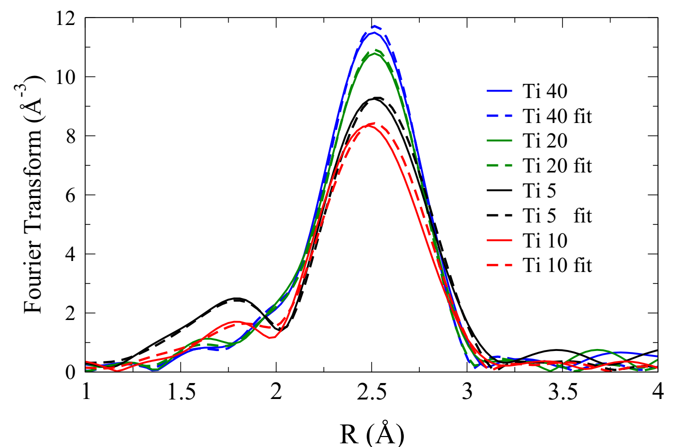

FIG. 8. Best-fit results at the Ti K edge for the as-deposited (AD) samples (broken curves) compared with the experimental FT signals (continuous curves).

TABLE II. Best-fit values of Ti-O and Ti-Ti NN distances and XAFS Debye–Waller factor σ^2 for the as-deposited (AD) and annealed (Ann) set of samples. We report the two values found for Ti-Ti distance in the same column (see text). The S_0^2 values were kept fixed at 0.7. Errors have been obtained from the diagonal of the fit covalence matrix. They are equal to or less than 0.02 Å for interatomic distances and 0.002 for σ^2 (Ti-O) and σ^2 (Ti-Ti).

Samples	Ti-O nm (Å)	Ti-Ti (Å)	σ^2 (Ti-O) (Å^2)	σ^2 (Ti-Ti) (Å^2)
Ti metal	2.07	2.89/2.95		
Ti 5 nm AD	2.11	2.91/2.97	0.006	0.011
Ti 10 nm AD	2.10	2.90/2.95	0.006	0.013
Ti 20 nm AD	2.08	2.88/2.93	0.006	0.010
Ti 40 nm AD		2.88/2.94	0.006	0.010
Ti 5 nm Ann	2.08	2.93/2.99	0.006	0.020
Ti 10 nm Ann	2.10	2.94/2.99	0.006	0.015
Ti 20 nm Ann	2.10	2.92/2.97	0.006	0.013
Ti 40 nm Ann		2.88/2.94	0.006	0.010

TABLE III. $x_{O_h(\mathrm{Ti})}$ is the percent of oxygen population in the octahedral interstitial sites of the Ti hexagonal lattice, $x_{O_v(\mathrm{Hf})}$ is the percent of oxygen vacancies in the first coordination shell of Hf, before (AD) and after (Ann) annealing obtained by fitting of EXAFS spectra at the Ti K edge and the Hf L_{III} edge. The errors are equal to or less than 10%. $x^{\mathrm{corr.}}_{O_h(\mathrm{Ti})}$ is $x_{O_h(\mathrm{Ti})}$ in the annealed samples (column 4) minus $x_{O_h(\mathrm{Ti})}$ in the AD samples (column 2), which is the net fraction of O atoms migrating into Ti due to annealing. $x^{\mathrm{equiv.}}_{O_v(\mathrm{Hf})}$ is the equivalent values of oxygen vacancies calculated as described in the text by using Eq. (2) and $x^{\mathrm{corr.}}_{O_h(\mathrm{Ti})}$.

Samples	$x_{O_h(\mathrm{Ti})}$ % AD	$x_{O_v(\mathrm{Hf})}$ % AD	$x_{O_h(\mathrm{Ti})}$ % Ann	$x^{\mathrm{corr.}}_{O_h(\mathrm{Ti})}$ % Ann	$x_{O_v(\mathrm{Hf})}$ % Ann	$x^{\mathrm{equiv.}}_{O_v(\mathrm{Hf})}$ % Ann
Ti 5 nm	23	0	21	≃0	04	≃0
Ti 10 nm	11	0	25	≃14	13	≃13
Ti 20 nm	4	0	25	≃21	28	≃37
Ti 40 nm	0	0	≃0	≃0		

to this model the Ti absorbers are surrounded at most by six oxygen atoms at a distance equal to 2.067 Å, six Ti atoms at 2.895 Å, and six Ti atoms at 2.950 Å.

We fit experimental phase and amplitudes to experimental data in k space in the range 2.8 to 10.5 Å^{-1} by refining the following parameters: the origin of photoelectron energy E_0, the interatomic Ti-O distances for the I shell, the Ti-Ti interatomic distances, the XAFS Debye–Waller factor σ^2, and an amplitude factor $x_{O_h(\mathrm{Ti})}$ multiplying the amplitude of the Ti-O-pair contribution. The overall EXAFS amplitude factor S_0^2 was fixed to 0.7. The best-fit results are reported in Table II and shown in Figs. 8 and 9 for the as-deposited and annealed samples, respectively. The E_0 best-fit values were close to 8 ± 1 eV for Ti-O and 7 ± 1 eV for Ti-Ti, and differences lower than 1.2 eV were found for the different samples. The main peak of the FT amplitude corresponds, according to the model mentioned above, to the contribution of twelve Ti atoms, six at 2.895 Å and six at 2.95 Å. The two subshell contributions are merged into a single FT peak due both to the limited k range of the EXAFS spectra and to the disordered nature of the Ti layer that introduces static disorder in the interatomic distances. Therefore, we refined a unique ΔR value that is applied to the reference distances of hexagonal Ti, as reported in Table II. The $x_{O_h(\mathrm{Ti})}$ value corresponds to the occupation fraction of the six O octahedral sites available in the hexagonal Ti lattice. Refining of this parameter quantifies the oxygen migration mechanism. The $x_{O_h(\mathrm{Ti})}$ values are reported in Table III. We see that the interatomic distances found for both Ti-O and Ti-Ti pairs for the as-deposited samples are in general very close to the values foreseen by the crystallographic structure used as a model, confirming the hypothesis of occupation of the octahedral sites in the Ti hexagonal lattice. Nevertheless, we see that they are slightly larger for the Ti 5 nm and Ti 10 nm samples, in agreement with an expansion of the Ti lattice due to the presence of O atoms in the O_h interstitial lattice sites. This is shown in Table III by the $x_{O_h(\mathrm{Ti})}$ parameter that is equal to 23% and 11% for the Ti 5 nm and Ti 10 nm samples, respectively. The O_h-site occupation number is practically negligible instead for the Ti 20 nm and Ti 40 nm samples for which the Ti-Ti distances are slightly shorter. Once the samples are annealed a strong increase of $x_{O_h(\mathrm{Ti})}$ is observed for the Ti 10 nm and Ti 20 nm samples together with an increase both of the DW factors and interatomic distances of Ti-Ti pairs, associated with the increased occupation factor of the O_h sites. For the Ti 40 nm sample these effects are practically negligible. For the Ti 5 nm sample the effect of the annealing is essentially an increase in structural disorder and there is almost no increase of $x_{O_h(\mathrm{Ti})}$. This is in qualitative agreement with the results found at the Hf L_{III} edge showing a release of O atoms from the Hf first O coordination shell. The percent of oxygen population in the Ti lattice O_h interstitial sites is reported in Table III and compared with the percent of oxygen vacancies in the first coordination shell of Hf ($x_{O_v(\mathrm{Hf})}$). One observes that the O atoms fraction lost by Hf does not correspond to the O atoms fraction gathered by Ti in the first coordination shell. This finding is discussed in Sec. V.

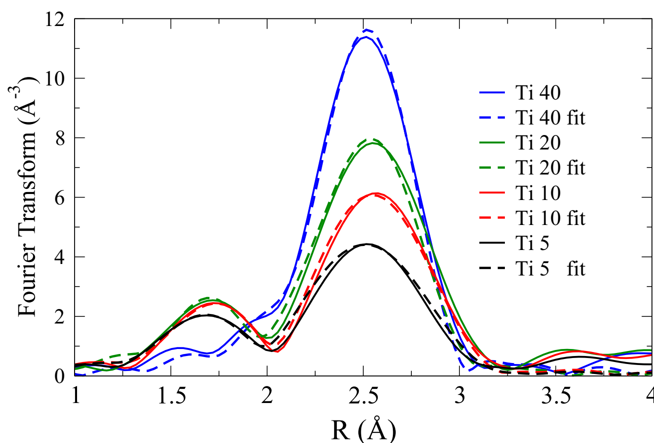

FIG. 9. Best-fit results at the Ti K edge for the annealed (Ann) samples (broken curves) compared with the experimental FT signals (continuous curves).

IV. X-RAY ABSORPTION NEAR-EDGE STRUCTURE

We show in Fig. 10 normalized x-ray absorption near edge structure (XANES) spectra at the Ti K and Hf L_{III} edges for the as-deposited and annealed set of samples. In general, the Ti-K-edge spectra are similar to the spectrum of Ti metal foil. The main difference is the atomic disorder that is larger in the Ti layers before annealing and further increases after annealing (see also Sec. III B). Interestingly, in Fig. 10, one can observe a noticeable decrease of the intensity of the A peak which appears at 4966.6 eV when decreasing the Ti layer thickness. Annealing further decreases the A peak intensity for the Ti 5 nm, Ti 10 nm, and Ti 20 nm samples. In addition, because its intensity is the same for the Ti 40 nm AD, Ti 40 nm Ann, and the Ti foil, one can say that it is weakly sensitive to structural disorder.

Ti atoms in Ti metal (electronic configuration: $3d^3 4s^1$) sit on the noncentrosymmetric position $2c$ (point group $\bar{6}m2$) which has no inversion symmetry, allowing the local hybridization of the Ti $3d$ and $4p$ orbitals. Therefore, the A feature intensity is ascribed mainly to the dipolar transition from the Ti $1s$ to $4p$ character of the $3d$ band [39–42]. From a qualitative point of view, one can state that the decrease of the A feature intensity results from a weaker hybridization; that is, the local environment of some of the Ti atoms tends to be more centrosymmetric due to the presence of oxygen atoms [41,42]. Oxygen can occupy both octahedral and tetrahedral interstitial sites in the wurtzite structure and when it occupies the octahedral sites, the Ti-atom environment becomes centrosymmetric. As a matter of fact, we demonstrate in Sec. III B that the oxygen atoms sit in the octahedral interstitial sites (O_h). On the other hand, for the Ti AD samples, one can see that the A-feature intensity increases linearly as a function of the Ti layer thickness to reach the maximum intensity observed for the Ti foil. This means that only a constant fraction of the Ti atoms is oxidized whatever the Ti thickness is, in agreement with the EXAFS results. Most likely, oxygen-atom diffusion is very low and takes place in a thin Ti layer close to the Ti/HfO_2 interface, in agreement with theoretical calculations [20,26].

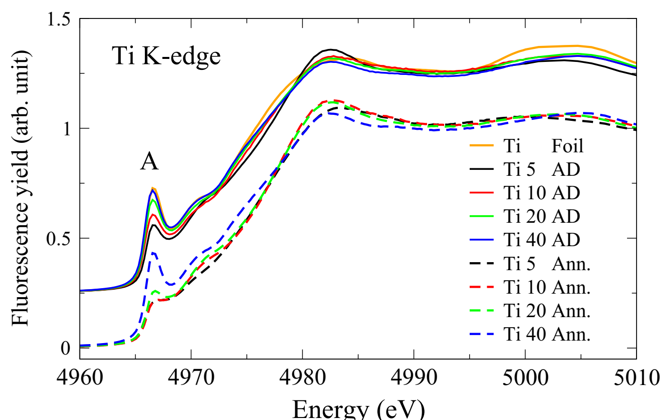

FIG. 10. XANES spectra at the Ti K edge of the as-deposited (AD, continuous curves) and annealed samples (Ann, broken curves) for the different Ti cap-layer thicknesses. The AD spectra are shifted by 0.25 along the y axis for clarity.

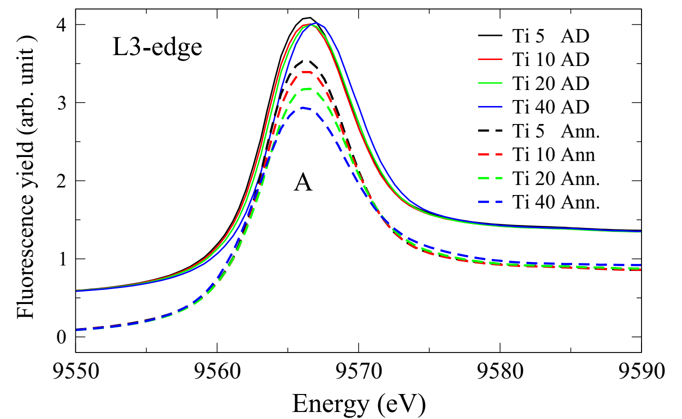

FIG. 11. XANES spectra at the Hf L_{III} edge of the as-deposited (AD, continuous curves) and annealed samples (Ann, broken curves) for the different Ti cap-layer thicknesses. The AD spectra are shifted by 0.5 along the y axis for clarity.

We show in Fig. 11 normalized XANES spectra at the Hf L_{III} edge for the as-deposited and annealed set of samples. The resonance line (white line) at 9566 eV (A feature) corresponds to the electronic transition from the deep Hf $2p_{3/2}$ core level to a rather sharp Hf $5d$ state band of the monoclinic HfO_2 [43]. Basically, the A peak area depends on the filling of the d band; the lower the filling the higher the intensity. Formally, the Hf^{+4} ion in HfO_2 has an empty $5d$ state $5d^0 6s^0$ and $Hf^{(4-\delta)}$ has a partially filled $5d$ state [38,44–46]. Regarding the as-deposited samples, Fig. 11 shows that there are almost no changes in the A-peak intensity whatever the Ti layer thickness is. This does not preclude any oxygen diffusion from HfO_2 to the Ti layer, but it concerns a too-small number of oxygen atoms to be detected by XAFS (less than a few percent). Hafnium remains in a 4+ oxidation state. Also, the absence of features on the right side of the A peak close to 9585 eV is identified as a signature of amorphous HfO_2 [38,45], which is in agreement with our XRD data. As for the annealed samples, one observes a decrease of the A-peak intensity when the Ti layer thickness increases. This is a clear indication that Hf ions undergo a reduction of the oxidation state which is most likely due to the oxygen diffusion towards the Ti layer. One can observe that the area difference between the A peaks of the Ti 5 nm and Ti 20 nm is about 2.2 times the area difference between the A peaks of the Ti 5 nm and Ti 10 nm. This is in fairly good agreement with the EXAFS results showing a doubling of the oxygen vacancies ($x_{O_v(Hf)}$ in Table III). It should be noticed that, for the Ti 40 nm sample, not only the A-peak intensity is lowered but the peak width increases, which may indicate a change in the Hf local environment.

V. DISCUSSION

The EXAFS results clearly show that an oxygen migration from HfO_2 into Ti capping occurs, the strength of which depends both on the Ti layer thickness and the sample thermal budget. The oxygen atoms migrate into the O_h interstitial site of Ti metal close to the Ti/HfO_2 interface, which corresponds to the lowest-energy interstitial position, in agreement with previous *ab initio* calculations [20,26]. In Table III we give the

experimental fractions of oxygen atoms in the O_h interstitial sites of the Ti lattice, $x_{O_h(Ti)}$, and oxygen vacancies in the Hf I shell, $x_{O_v(Hf)}$, as determined by the EXAFS curves fitting for the as-deposited (AD) and annealed (Ann) samples. We also report as $x^{equiv.}_{O_v(Hf)}$ the equivalent fraction of oxygen atoms that should leave the Hf I coordination shell to migrate to the Ti cap layer and produce the O concentration $x_{O_h(Ti)}$ observed by EXAFS at the Ti K edge. These values ($x^{equiv.}_{O_v(Hf)}$) were obtained by normalizing the migrated-oxygen amount to the absolute cation numbers, Hf and Ti, contained by the HfO_2 and Ti layers, respectively, taking into account the different sample thickness and the lattice volume ratio of hexagonal Ti to monoclinic HfO_2. We also take into account the oxygen coordination by considering that oxygen in Ti metal O_h sites is coordinated to six Ti atoms (and Ti atoms are coordinated to six O atoms). In the case of HfO_2 instead, there exist two kinds of O atoms in the Hf I shell: three O atoms (out of seven) are coordinated to three Hf atoms and four are coordinated to four Hf atoms. Therefore $x^{equiv.}_{O_v(Hf)}$ is given by

$$x^{equiv.}_{O_v(Hf)} = \frac{1}{2}\frac{n_{Ti}}{n_{HfO_2}}\frac{t_{Ti}}{t_{HfO_2}}x_{O_h(Ti)}, \tag{2}$$

where $n_{Ti} = 9.4 \times 10^{-2}$ mol/cm^3 and $n_{HfO_2} = 4.6 \pm 0.55 \times 10^{-2}$ mol/cm^3 are the numbers of Ti and Hf atoms per volume unit, respectively; t_{Ti} and $t_{HfO_2} = 9.3 \pm 0.15$ nm are the Ti and HfO_2 film thicknesses, respectively; $x_{O_h(Ti)}$ is the experimental fraction of oxygen atoms in the Ti I O_h shell. The experimental values of t_{HfO_2} and n_{HfO_2} were obtained by XRR measurements, those of t_{Ti} by TEM, $t_{Ti} = 5$, 10, and 19 nm for Ti 5 nm, Ti 10 nm, and Ti 20 nm samples, respectively; n_{Ti} is the bulk value for α-Ti.

In the case of as-deposited samples, the O_h oxygen site occupancy is equal to 21% and 11% for the Ti 5 nm and Ti 10 nm, respectively. This means that a consistent amount of oxygen is diffused into Ti capping even before any thermal treatment. In addition, the absolute amount of O atoms keeps constant when doubling the Ti cap thickness since the O percentage is reduced by a factor of two. It should scale down to 5% and 2% for the Ti 20 nm and Ti 40 nm samples, respectively, but these values are of the same order as the EXAFS sensitivity to composition and, as shown in Table III, the O fraction for these two samples is found to be negligible. This suggests that a constant number of oxygen atoms is present in the Ti metal layer whatever the layer thickness is. It has to be noticed that a large number of O atoms in the Ti 5 nm sample cannot be explained by the interface oxygen atoms shared by Hf and Ti. The Hf-O-Ti interface region, even considering the amorphous nature of the samples, can span at most over two monolayers, representing no more than the 10% of the whole Ti thickness. Since the oxygen diffusion into Ti metal is kinetically limited [20,26], it is very likely that Ti oxidation takes place close to the interface, in agreement with previous experimental x-ray photoelectron spectroscopy findings [47]. In addition, EXAFS results at the Hf K edge show that the number of oxygen vacancies, $x_{O_v(Hf)}$, in the HfO_2 film is under the detection limit. Then, from Eq. (2), one can say that such a large number of O atoms in the Ti layer are not from the Hf nearest-neighbor shell. We believe that they are mainly from the oxido-reaction involving Ti and H_2O molecules present at the surface of the HfO_2 layer and trapped inside. This does not rule out some weak oxygen depletion in a very thin HfO_2 layer close to the Ti/HfO_2 interface [9,20].

In the case of annealed samples, striking experimental results are observed. The annealing does not modify the oxygen content ($x_{O_h(Ti)}$) in the Ti 5 nm (21%) and the number of oxygen vacancies in HfO_2 ($x_{O_v(Hf)}$ in Table III) stays very low (a few percent). Only σ^2 (Ti-Ti), the static disorder of the Ti-Ti distance, increases notably, as reported in Table II, showing that the annealed Ti 5 nm is the most disordered layer. This suggests that the annealing effect is to spread the O atoms from the interface region to a thicker-layer region, producing Ti lattice disorder. This increase in static disorder could also be due to some other structural change produced by annealing. Indeed, Fig. 1(d) shows a Pt interdiffusion at the Pt/Ti interface of the Ti 10 nm; nevertheless, EXAFS does not detect Pt atoms as Ti neighbors, showing that Pt/Ti intermixing is limited to the near-interface region. This is corroborated by XRR results. When the Ti thickness increases, the O_h oxygen site occupancy increases and reaches 25% for Ti 10 nm and Ti 20 nm samples, whereas it is close to zero for Ti 40 nm. Concomitantly, one observes a decrease of the static disorder that must be due to the presence of a larger unperturbed Ti-lattice region, i.e., not O enriched. This provides a clear indication that, during the annealing, the O atoms do not diffuse into the whole Ti layer in a uniform way but show a concentration gradient from the interface to the top region. We have shown in the XANES Sec. IV that Ti layers retain the α-Ti hexagonal compact structure (hcp) upon annealing. At 400 °C several hcp suboxides can exist with different ordering of the oxygen atoms in the O_h sites [27]. According to the Ti-O phase diagram [27], the maximum oxygen occupancy in α-Ti is 50% (half of the O_h sites are filled), which corresponds to the stoichiometry of Ti_2O (α-Ti has the same number of Ti and O_h sites). A 25% O_h interstitial site occupancy would correspond to the stoichiometry of Ti_3O. Since the EXAFS O_h site occupancy equal to 25% is an average value, it could correspond either to a homogeneous Ti_3O suboxide or to the existence of Ti_2O close to the Ti/HfO_2 interface, together with an upper oxygen poor and/or free α-Ti layer [20].

In Table III, we see that the amount of oxygen vacancies in HfO_2 ($x_{O_v(Hf)}$) starts to increase significantly when the Ti layer thickness increases; it reaches 13% for Ti 10 nm and 28% for Ti 20 nm samples. For comparing the number of oxygen atoms which diffuse in the Ti layer during the annealing with the number of oxygen vacancies in the Hf I coordination shell, one needs first to subtract the number of oxygen atoms present in the Ti layer prior to annealing. The obtained values are reported in Table III as $x^{corr.}_{O_h(Ti)}$. We find 0%, 14%, and 21% for the Ti 5 nm, Ti 10 nm, and Ti 20 nm samples, respectively. Then, these values ($x^{corr.}_{O_h(Ti)}$) were used to calculate $x^{equiv.}_{O_v(Hf)}$ with Eq. (2), the latter represents the equivalent fraction of oxygen atoms that should leave the Hf environment to diffuse into Ti due to the annealing, according to an ideal model dealing with α-Ti metal and crystalline m-HfO_2. The $x^{equiv.}_{O_v(Hf)}$ values have to be compared with the oxygen vacancy fraction $x_{O_v(Hf)}$ observed by EXAFS. We see a rather good agreement for the Ti 5 nm and Ti 10 nm samples, i.e., increasing the Ti cap thickness increases the amount of oxygen gettered out of the HfO_2 layer to the Ti layer, the extent of which is quantified by EXAFS. For

the Ti 20 nm sample, the $x^{\text{equiv.}}_{O_v(\text{Hf})}$ value is about 10% higher than $x_{O_v(\text{Hf})}$, which is slightly larger than the EXAFS error bar. This could indicate that some amount of the oxygen atoms enriching the Ti cap after annealing do not come from the m-HfO_2 layer as is hypothesized in Eq. (2). We can exclude that this excess is due to some O atoms coming from top oxidized Ti during annealing since a 40-nm-thick Pt top layer was deposited onto Ti to prevent such an effect. Also, the rather small discrepancy cannot be attributed to an intermixing or roughening at the Ti/HfO_2 interface, which would increase the O atoms in the interface Ti environment without oxygen diffusion, since both XRR and TEM results show that the Ti/HfO_2 interface is not affected. Some authors [48,49] attributed the presence of O atoms in the Ti layer after a mild annealing at 300 °C in forming gas of Ti/HfO_2/Si stacks, to the diffusion of O from the very thin SiO_2 layer present on top of the silicon substrate. Although in the present study the HfO_2 layers are about three times thicker than those of the above-mentioned papers, the migration of O atoms from the SiO_2 layer cannot be excluded. It would lead to the overestimation of the number of oxygen atoms that truly migrated from the Hf local environment, in the calculation of the equivalent oxygen vacancies ($x^{\text{equiv.}}_{O_v(\text{Hf})}$). Coming to that point, we must underline first, that Eq. (2) is an oversimplified model valid for crystalline α-Ti metal and m-HfO_2. In our case the HfO_2 is amorphous and the Ti layer only partially ordered with nanodomains coexisting with amorphous materials [Figs. 1(a) and 1(b)], second, that in general the EXAFS sensitivity to coordination number is limited and its error bar is easily in the range [10%–20%]. Therefore, we believe that the model, although perfectible, is very likely to support our general interpretation.

In summary, x-ray absorption spectroscopy (XAS) at the Ti K edge and Hf L_{III} edge has been performed on samples as deposited and annealed in Ar at 400 °C for one hour. This study combines EXAFS and XANES measured at both the Hf and Ti edges. The results are all in fair agreement and give a direct view at a local scale of the oxygen migration mechanism. We quantified the migration of O from HfO_2 to Ti, promoted by annealing. The nature of the getter mechanism is understood by comparing samples with increasing Ti capping thickness. We show that the Ti getter effect has to be activated by thermal treatment and that the O diffusion takes place in a region of a few nanometers close to the Ti/HfO_2 interface.

ACKNOWLEDGMENTS

R.V. was supported by the LabEx MINOS ANR-10-LABX-55-01. We acknowledge the French CRG (ESRF) and ESRF for granting beam time at beamline BM30-FAME (proposal number MA2383). We are grateful to the BM30-FAME staff, in particular to D. Testemale, for technical support and assistance during the experiment. We acknowledge Dr. P. Gonon from the *Laboratoire des Technologies de la Microélectronique* (LTM) for the critical reading of our manuscript. M.G.P. acknowledges the support of project MAT 2015-66726-R of the Spanish Ministry of Science and Innovation and is grateful to the Diputación General de Aragón for granting support in the frame of the Researchers Mobility program (Grant No. 224-183). Sample preparation has required the access to the *Plateforme Technologique Amont* of Grenoble which is supported by the Nanosciences Fondation and CNRS Renatech network. Transmission electron microscopy was performed at the CMTC characterization platform of Grenoble INP supported by the Centre of Excellence of Multifunctional Architectured Materials CEMAM ANR-10-LABX-44-01 funded by the Investments for the Future Program.

[1] I. Baek, M. Lee, S. Seo, M. Lee, D. Seo, D.-S. Suh, J. Park, S. Park, H. Kim, I. Yoo *et al.*, in *Electron Devices Meeting, 2004. IEDM Technical Digest, IEEE International* (IEEE, 2004), pp. 587–590.

[2] H.-S. P. Wong, H.-Y. Lee, S. Yu, Y.-S. Chen, Y. Wu, P.-S. Chen, B. Lee, F. T. Chen, and M.-J. Tsai, Proc. IEEE **100**, 1951 (2012).

[3] Y. Chen, H. Lee, P. Chen, P. Gu, C. Chen, W. Lin, W. Liu, Y. Hsu, S. Sheu, P. Chiang *et al.*, in *Electron Devices Meeting (IEDM), 2009 IEEE International* (IEEE, 2009), pp. 1–4.

[4] Y. S. Chen, H. Y. Lee, P. S. Chen, C. H. Tsai, P. Y. Gu, T. Y. Wu, K. H. Tsai, S. S. Sheu, W. P. Lin, C. H. Lin, P. F. Chiu, W. S. Chen, F. T. Chen, C. Lien, and M.-J. Tsai, *Electron Devices Meeting (IEDM), 2011 IEEE International* (IEEE, 2011), pp. 31.3.1–31.3.4.

[5] G. He, Z. Sun, G. Li, and L. Zhang, Crit. Rev. Solid State Mater. Sci. **37**, 131 (2012).

[6] B. Govoreanu, G. Kar, Y.-Y. Chen, V. Paraschiv, S. Kubicek, A. Fantini, I. Radu, L. Goux, S. Clima, R. Degraeve, N. Jossart, O. Richard, T. Vandeweyer, K. Seo, P. Hendrickx, G. Pourtois, H. Bender, L. Altimime, D. Wouters, J. Kittl, and M. Jurczak, *Electron Devices Meeting (IEDM), 2011 IEEE International* (IEEE, 2011), pp. 31.6.1–31.6.4.

[7] R. Waser, R. Dittmann, G. Staikov, and K. Szot, Adv. Mater. **21**, 2632 (2009).

[8] Z. Wei, Y. Kanzawa, K. Arita, Y. Katoh, K. Kawai, S. Muraoka, S. Mitani, S. Fujii, K. Katayama, M. Iijima, T. Mikawa, T. Ninomiya, R. Miyanaga, Y. Kawashima, K. Tsuji, A. Himeno, T. Okada, R. Azuma, K. Shimakawa, H. Sugaya, T. Takagi, R. Yasuhara, K. Horiba, H. Kumigashira, and M. Oshima, *Electron Devices Meeting (IEDM), 2008 IEEE International* (IEEE, 2008), pp. 1–4.

[9] M. Sowinska, T. Bertaud, D. Walczyk, S. Thiess, M. Schubert, M. Lukosius, W. Drube, C. Walczyk, and T. Schroeder, Appl. Phys. Lett. **100**, 233509 (2012).

[10] B. Traoré, K.-H. Xue, E. Vianello, G. Molas, P. Blaise, B. De Salvo, A. Padovani, O. Pirrotta, L. Larcher, L. Fonseca *et al.*, in *Reliability Physics Symposium (IRPS), 2013 IEEE International* (IEEE, 2013), pp. 5E–2.

[11] S.-S. Sheu, M.-F. Chang, K.-F. Lin, C.-W. Wu, Y.-S. Chen, P.-F. Chiu, C.-C. Kuo, Y.-S. Yang, P.-C. Chiang, W.-P. Lin *et al.*, in *Solid-State Circuits Conference Digest of Technical Papers (ISSCC), 2011 IEEE International* (IEEE, 2011), pp. 200–202.

[12] H. Lee, Y. Chen, P. Chen, T. Wu, F. Chen, C. Wang, P. Tzeng, M.-J. Tsai, and C. Lien, IEEE Electron Device Lett. **31**, 44 (2010).

[13] E. Vianello, O. Thomas, G. Molas, O. Turkyilmaz, N. Jovanović, D. Garbin, G. Palma, M. Alayan, C. Nguyen, J. Coignus *et al.*,

in *Electron Devices Meeting (IEDM), 2014 IEEE International* (IEEE, 2014), pp. 6.3.1–6.3.4.
[14] R. Waser, *Nanoelectronics and Information Technology* (John Wiley & Sons, 2012).
[15] D. Ielmini, Semicond. Sci. Technol. **31**, 063002 (2016).
[16] P. Gonon, M. Mougenot, C. Vallée, C. Jorel, V. Jousseaume, H. Grampeix, and F. El Kamel, J. Appl. Phys. **107**, 074507 (2010).
[17] S. Sharath, T. Bertaud, J. Kurian, E. Hildebrandt, C. Walczyk, P. Calka, P. Zaumseil, M. Sowinska, D. Walczyk, A. Gloskovskii *et al.*, Appl. Phys. Lett. **104**, 063502 (2014).
[18] P. Calka, E. Martinez, V. Delaye, D. Lafond, G. Audoit, D. Mariolle, N. Chevalier, H. Grampeix, C. Cagli, V. Jousseaume *et al.*, Nanotechnol. **24**, 085706 (2013).
[19] X. Cartoixà, R. Rurali, and J. Suñé, Phys. Rev. B **86**, 165445 (2012).
[20] B. Traoré, P. Blaise, E. Vianello, L. Perniola, B. De Salvo, and Y. Nishi, IEEE Trans. Electron Devices **63**, 360 (2016).
[21] A. Padovani, L. Larcher, P. Padovani, C. Cagli, and B. De Salvo, in *Memory Workshop (IMW), 2012 4th IEEE International* (IEEE, 2012), pp. 1–4.
[22] H. Lee, P. Chen, T. Wu, Y. Chen, C. Wang, P. Tzeng, C. Lin, F. Chen, C. Lien, and M.-J. Tsai, in *Electron Devices Meeting, 2008. IEDM 2008. IEEE International* (IEEE, 2008), pp. 1–4.
[23] K. G. Young-Fisher, G. Bersuker, B. Butcher, A. Padovani, L. Larcher, D. Veksler, and D. C. Gilmer, IEEE Electron Device Lett. **34**, 750 (2013).
[24] B. Traoré, P. Blaise, and B. Sklénard, J. Phys. Chem. C **120**, 25023 (2016).
[25] P. Calka, M. Sowinska, T. Bertaud, D. Walczyk, J. Dabrowski, P. Zaumseil, C. Walczyk, A. Gloskovskii, X. Cartoixà, J. Suñé, and T. Schroeder, ACS Appl. Mater. Interfaces **6**, 5056 (2014).
[26] H. H. Wu and D. R. Trinkle, Phys. Rev. Lett. **107**, 045504 (2011).
[27] J. Murray and H. Wriedt, J. Phase Equilib. **8**, 148 (1987).
[28] F. Boscherini, in *Characterization of Semiconductor Heterostructures and Nanostructures II*, edited by G. Agostini and C. E. Lamberti (Elsevier, Amsterdam, 2012), Chap. 7.
[29] P. Calka, E. Martinez, D. Lafond, H. Dansas, S. Tirano, V. Jousseaume, F. Bertin, and C. Guedj, Microelectron. Eng. **88**, 1140 (2011).
[30] A. L. Ankudinov, B. Ravel, J. J. Rehr, and S. D. Conradson, Phys. Rev. B **58**, 7565 (1998).
[31] B. Ravel and M. Newville, J. Synchrotron Radiat. **12**, 537 (2005).
[32] X. Zhao and D. Vanderbilt, Phys. Rev. B **65**, 233106 (2002).
[33] B. Ravel, J. Synchrotron Radiat. **8**, 314 (2001).
[34] J. Adam and M. D. Rogers, Acta Crystallogr. **12**, 951 (1959).
[35] R. E. Hann, P. R. Suitch, and J. L. Pentecost, J. Am. Ceram. Soc. **68**, C-285 (1985).
[36] P. S. Lysaght, J. C. Woicik, M. Alper Sahiner, B.-H. Lee, and R. Jammy, Appl. Phys. Lett. **91**, 122910 (2007).
[37] P. S. Lysaght, J. C. Woicik, M. A. Sahiner, B.-H. Lee, and R. Jammy, J. Non-Cryst. Solids **354**, 399 (2008).
[38] D.-Y. Cho, T. J. Park, K. D. Na, J. H. Kim, and C. S. Hwang, Phys. Rev. B **78**, 132102 (2008).
[39] F. de Groot, G. Vankó, and P. Glatzel, J. Phys.: Condens. Matter **21**, 104207 (2009).
[40] A. Balzarotti, M. De Crescenzi, and L. Incoccia, Phys. Rev. B **25**, 6349 (1982).
[41] F. Farges, G. E. Brown, and J. J. Rehr, Phys. Rev. B **56**, 1809 (1997).
[42] T. Yamamoto, X-Ray Spectrom. **37**, 572 (2008).
[43] P. W. Peacock and J. Robertson, J. Appl. Phys. **92**, 4712 (2002).
[44] F. W. Lytle, P. S. P. Wei, R. B. Greegor, G. H. Via, and J. H. Sinfelt, J. Chem. Phys. **70**, 4849 (1979).
[45] J. Morais, L. Miotti, K. P. Bastos, S. R. Teixeira, I. J. R. Baumvol, A. L. P. Rotondaro, J. J. Chambers, M. R. Visokay, L. Colombo, and M. C. M. Alves, Appl. Phys. Lett. **86**, 212906 (2005).
[46] D.-Y. Cho, J.-M. Lee, S.-J. Oh, H. Jang, J.-Y. Kim, J.-H. Park, and A. Tanaka, Phys. Rev. B **76**, 165411 (2007).
[47] M. Sowinska, T. Bertaud, D. Walczyk, S. Thiess, P. Calka, L. Alff, C. Walczyk, and T. Schroeder, J. Appl. Phys. **115**, 204509 (2014).
[48] L. V. Goncharova, M. Dalponte, T. Gustafsson, O. Celik, E. Garfunkel, P. S. Lysaght, and G. Bersuker, J. Vac. Sci. Technol., A **25**, 261 (2007).
[49] H. Kim, P. C. McIntyre, C. On Chui, K. C. Saraswat, and S. Stemmer, J. Appl. Phys. **96**, 3467 (2004).